Appendix 1

Regions of interest in quantitative image analysis

For drawing the circular region of interest (ROI), the liver attenuation values were calculated by averaging four measurements for each of the four liver sections: the left lateral, left medial, right anterior, and right posterior sections. A single ROI was measured on other anatomic structures: the paraspinal muscle, portal vein, and subcutaneous fat (*Figure S1*). All ovoid ROIs (range, 100–200 mm^2) were carefully placed in the areas of homogeneous attenuation to avoid confounding structures such as large vessels, intramuscular fat, and vessel wall calcifications. All measurements were performed at the level of the portal vein. For pancreatic CT number measurements, the mean CT number was obtained using an ROI drawn at a spared portion of pancreatic parenchyma with care being taken to avoid the main pancreatic duct, visible vessels, and artifacts. The mean CT attenuation of the lung field was measured by placing a round ROI (approximately 50–200 mm^2) between the pulmonary nodule and adjacent lung parenchyma. Image noise was defined as the standard deviation of the HU in a homogeneous region of the subcutaneous fat on the anterior abdominal wall away from artefact or vessels. The manual measurements of the lymph node size were performed in the transversal plane with two perpendicular diameters: the long and short axis of the lymph node. Lymph nodes were divided into two groups according to the Response Evaluation Criteria in Solid Tumors (RECIST) 1.1 criteria for assessment as follows: less than 10 mm in the short axis and 10 mm and more in the short axis. For all measures, the size, shape, and position of the ROI were kept consistent and were obtained three times at different image levels, with the average values being calculated.

Appendix 2

Low- and high-contrast lesions

For the analysis of lesions, the liver lesions were further divided into low- and high-contrast lesions based on the CT attenuation relative to surrounding tissues. Low-contrast lesions are characterized by a small difference in attenuation between the lesion and the surrounding environment with an average of approximately 15 HU for the contrast level or with contrasts in the range of 12–40 HU in several phantom-based studies (26,32). The detection of low-contrast lesions in CT is challenging. On the other hand, high-contrast lesions exhibit a significant disparity in attenuation when compared to the surrounding tissues, with a lesion-to-background difference ≥100 HU (33). Herein, we variably refer to lesions as low contrast (i.e., hepatic cyst and hypovascular hepatic metastases) or high contrast (i.e., hepatic hemangioma and hypervascular hepatocellular carcinoma).

Appendix 3

Results of lesion detectability

For pulmonary nodules, both SD protocol and LD protocols could provide full detectability on all 88 pulmonary nodules (size classification: 31 nodules ≤0.5 cm, 39 nodules between 0.6–1.0 cm, and 18 nodules >1.0 cm; type classification: 81 solid nodules, 3 subsolid nodules, and 4 calcified nodules).

For liver lesions, the detection rate in LD-$DL_{50\ keV}$ VMIs was lower than that in SD-$IR_{50\ keV}$ and LD-$DL_{40\ keV}$ VMIs (87.7% *vs.* 99.1% and 92.0%; P <0.001). The difference was mainly in the detection of small or low-contrast liver lesions. The detection rates for small liver lesions (≤0.5 cm) was lower in LD-$DL_{50\ keV}$ VMIs (43/65, 66.2%) than that in SD-$IR_{50\ keV}$ (63/65, 96.9%; P <0.001) and LD-$DL_{40\ keV}$ VMIs (51/65, 78.5%; P <0.05). In the comparison to SD-$IR_{50\ keV}$ VMIs, no difference was found in LD-$DL_{50\ keV}$ or LD-$DL_{40\ keV}$ VMIs for detecting liver lesions of size at between 0.6 and 1.0 cm [38/38 (100%) *vs.* 35/38 (192.1%) *vs.* 36/38 (94.7%); P>0.05] or >1.0 cm [109/109 (100%) *vs.* 108/109 (99.1%) *vs.* 108/109 (99.1%); P>0.05]. The detection rate for low-contrast liver lesions was lower in LD-$DL_{50\ keV}$ VMIs [174/200, 87.0%) than in SD-$IR_{50\ keV}$ and LD-$DL_{40\ keV}$ VMIs (198/200 (99.0%) and 183/200 (91.5%); P<0.001). No difference was found in the detection of high-contrast liver lesions (12/12, 100%; P >0.05).

Regarding lymph nodes, the detection rates in the VMIs of LD-$DL_{50\ keV}$ (123/126, 97.6%) and LD-$DL_{40\ keV}$ VMIs (124/126,

https://dx.doi.org/10.21037/qims-24-197

98.4%) were comparable to that in SD-$IR_{50\ keV}$ VMIs (125/126, 99.2%) (P>0.05). No difference was found for the detection of lymph nodes of different size (≤1.0 and >1.0 cm) or type (axillary, mediastinal, retroperitoneal, and inguinal).

References

32. Toia GV, Zamora DA, Singleton M, Liu A, Tan E, Leng S, Shuman WP, Kanal KM, Mileto A. Detectability of Small Low-Attenuation Lesions With Deep Learning CT Image Reconstruction: A 24-Reader Phantom Study. AJR Am J Roentgenol 2023;220:283-95.
33. Inoue A, Voss BA, Lee NJ, Takahashi H, Kozaka K, Heiken JP, Ehman EC, Vasconcelos R, Fidler JL, Lee YS, Mileto A, Johnson MP, Baer-Beck M, Weber NM, Michalak GJ, Halaweish A, Carter RE, McCollough CH, Fletcher JG. Diagnostic Performance in Low- and High-Contrast Tasks of an Image-Based Denoising Algorithm Applied to Radiation Dose-Reduced Multiphase Abdominal CT Examinations. AJR Am J Roentgenol 2023;220:73-85.

Table S1 Lesion characteristics

Parameter	No. of lesions/no. of patients	Size (cm)*
Pulmonary nodules	88/13	0.85±0.32
Subsolid nodules	3/2	0.67±0.15
Solid nodules (including pulmonary metastasis)	81/13	0.89±0.48
Calcified nodules	4/3	0.79±0.52
Liver lesions	210/32	2.60±1.71
Low-contrast lesions	198/32	2.27±1.31
Hepatic cyst	26/9	2.18±1.10
Hepatic metastases	172/24	2.37±1.41
High-contrast lesions	12/9	3.50±2.74
Hepatic hemangioma	4/4	2.16±1.59
Hepatocellular	8/6	4.33±3.62
Lymph nodes	125/25	1.39±0.43
Axillary lymph nodes	12/4	0.90±0.30
Mediastinal lymph nodes	20/8	1.59±0.43
Retroperitoneal lymph nodes	80/12	2.25±4.45
Inguinal lymph nodes	13/5	0.95±0.31

*, data are the mean ± standard deviation.

https://dx.doi.org/10.21037/qims-24-197

Table S2 Subjective scores of image quality for the two readers

Subjective score (n=56)	Reader 1			Reader 2		
	$SD\text{-}IR_{50\ keV}$	$LD\text{-}DL_{50\ keV}$	$LD\text{-}DL_{40\ keV}$	$SD\text{-}IR_{50\ keV}$	$LD\text{-}DL_{50\ keV}$	$LD\text{-}DL_{40\ keV}$
Image noise						
1	0	0	0	0	0	0
2	0	0	0	0	0	0
3	22	14	24	19	14	22
4	12	24	22	13	24	24
5	22	18	10	24	18	10
Vessel conspicuity						
1	0	0	0	0	0	0
2	0	0	0	0	0	0
3	9	11	4	7	10	4
4	30	30	29	31	33	28
5	17	15	23	18	13	24
Image contrast						
1	0	0	0	0	0	0
2	0	0	0	0	0	0
3	0	2	1	0	0	1
4	23	21	15	19	20	13
5	33	33	40	37	36	42
Artificial sensation						
1	0	0	0	0	0	0
2	0	0	0	0	0	0
3	6	9	15	5	11	14
4	32	31	29	33	30	30
5	18	16	12	18	15	12
Overall image quality						
1	0	0	0	0	0	0
2	0	0	0	0	0	0
3	11	11	14	9	10	15
4	31	30	27	33	33	27
5	14	15	15	14	13	14

$SD\text{-}IR_{50\ keV}$, standard-dose 50-keV virtual monochromatic images with iterative reconstruction; $LD\text{-}DL_{50\ keV}$, low-dose 50-keV virtual monochromatic images with DLIR-H; $LD\text{-}DL_{40\ keV}$, low-dose 40-keV virtual monochromatic images with DLIR-H; DLIR-H, deep learning image reconstruction at high strength.

https://dx.doi.org/10.21037/qims-24-197

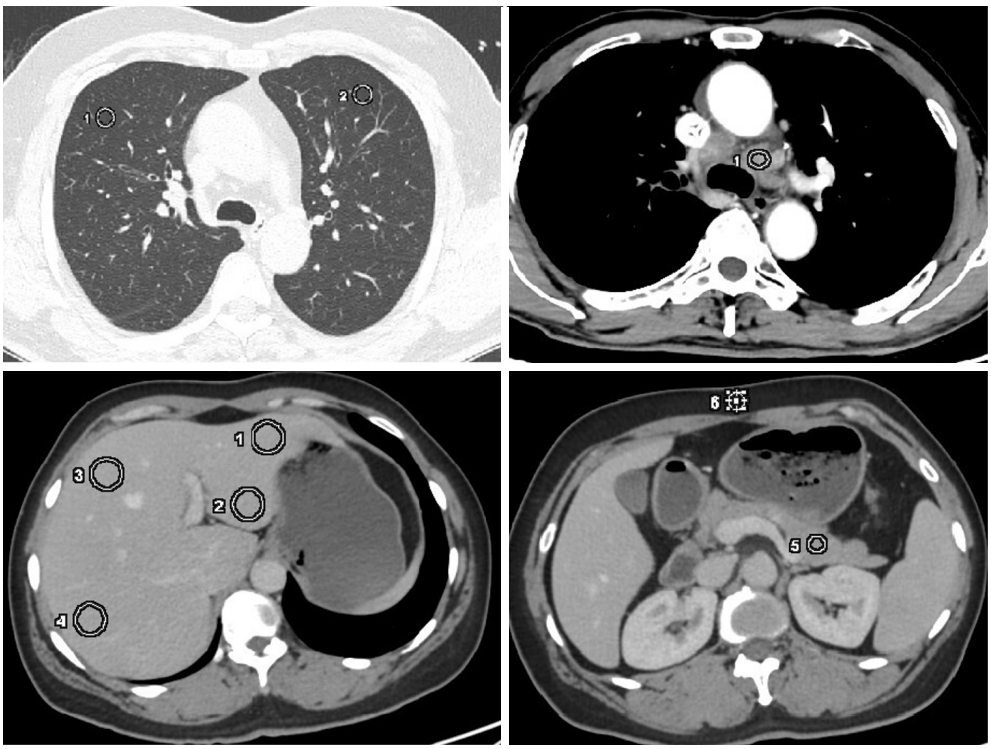

Figure S1 An illustrative example of a ROI measurements for the computed tomography attenuation and standard deviation. Each white circle indicates the placement and size of the ROI. ROI, region of interest.

https://dx.doi.org/10.21037/qims-24-197